



Fracture toughness characterization of single-crystalline tungsten using notched micro-cantilever specimens



C. Bohnert ^{a, b}, N.J. Schmitt ^b, S.M. Weygand ^{a, *}, O. Kraft ^b, R. Schwaiger ^b

^a Faculty of Mechanical Engineering and Mechatronics (MMT), Karlsruhe University of Applied Sciences, 76133 Karlsruhe, Germany

^b Institute for Applied Materials (IAM), Karlsruhe Institute of Technology (KIT), 76344 Eggenstein-Leopoldshafen, Germany

ARTICLE INFO

Article history:

Received 20 October 2015

Received in revised form 28 December 2015

Available online 8 February 2016

Keywords:

- A. Microcracking
- A. Stress intensity factor
- A. Fracture toughness
- C. Finite elements
- B. Crystal plasticity

ABSTRACT

The fracture toughness of tungsten is strongly influenced by microstructural features including crystal orientation and grain structure as well as specimen or component size. In order to gain insight into the mechanical response of individual grains, an experimental study using small scale fracture specimens was conducted and closely accompanied by finite element simulations. Free-standing notched single-crystalline tungsten micro-bending beams with an orientation of the $\{011\}\langle 0\bar{1}1 \rangle$ -crack system along the loading direction were loaded using a nanoindenter and modelled using crystal plasticity and cohesive zones. This combined numerical and experimental approach successfully demonstrates a procedure to determine the fracture toughness of such small non-standard specimens despite the occurrence of plastic deformation.

© 2016 Elsevier Ltd. All rights reserved.

1. Introduction

Tungsten as the metal with the highest melting point has a number of outstanding mechanical and physical properties and is considered as a structural material in current and future high-temperature energy conversion systems. In those applications, material robustness, i.e. high strength in combination with sufficient toughness, is absolutely critical. Therefore, improving the fracture toughness of components made from tungsten represents the most important challenge since the brittle-to-ductile transition of tungsten is well above room temperature.

Previous studies have shown that the fracture toughness of single-crystalline tungsten depends on the crystal orientation and the active crack system (Riedle et al., 1996; Gumbsch, 2003). For polycrystalline samples, it was demonstrated that the toughness strongly depends on microstructural characteristics such as grain size and shape, and texture (Gludovatz et al., 2010; Rupp and Weygand, 2010) with crack propagation typically observed to occur along grain boundaries. Thus, extruded tungsten with elongated grains is highly anisotropic and exhibits significantly improved toughness for cracking perpendicular to the preferred grain orientation (Riedle et al., 1996). On the other hand, results from bending tests by Reiser et al. (2013) show ductile behavior of ultrafine-grained tungsten at room temperature. It was suggested (Reiser et al., 2013) that the ductility of the tungsten foils is possibly caused by (i) the high amount of mobile edge dislocations, (ii) the ultra-fine grain size, and (iii) the foil effect which leads to dislocation annihilation at the free surfaces. Interestingly, the ductility of the foil disappeared after a heat treatment, which led to recrystallization and grain growth pointing to the ultra-fine grain size as key for the observed behavior. Thus, it can be concluded that grain boundaries are not inherently brittle, and the

* Corresponding author. Tel.: +49 721 925 1757 Fax: +49 721 925 1915.

E-mail address: sabine.weygand@hs-karlsruhe.de (S.M. Weygand).

macroscopically observed toughness is the result of the interplay between plasticity within grains and inter- or intra-crystalline crack propagation. In order to gain a deeper fundamental understanding of these mechanisms, the study of the fracture behavior of bi-crystalline sample is desirable. However, these should be conducted at an appropriate scale since size effects are known to strongly influence the deformation behavior in general (Kraft et al., 2010) and for the case of body-centered cubic (bcc) metals in particular (Kaufmann et al., 2011). Furthermore, for un-recrystallized swaged, extruded or rolled cylindrical rods made from tungsten, the grain size is typically of the order of several tens of microns in the elongated direction with an aspect ratio of the order of 4:1 (Margevicius et al., 1999), which requires fracture studies at this length scale and with a view to the application a micromechanical framework for describing the fracture behavior of tungsten.

In the literature, measurements of the fracture toughness on brittle materials have been reported using small-scale beam bending and focused ion beam-prepared notches since the last century. Notch geometries included double edge notches (Kraft et al., 1998) as well as top-down straight notches (Takashima et al., 2001). More recently, chevron notches were suggested as a means to reduce Ga contamination from the ion milling process and to promote a more stable crack growth (Mueller et al., 2015; Schmitt et al., 2013). Ion milling from the side represents another approach to minimize Ga implantation in the region of the crack (Kupka and Lilleodden, 2011). However, only few fracture-mechanical studies of metallic samples at the micro-scale have been reported. Wurster et al. (2012) performed fracture experiments using micrometer-sized notched cantilevers to study the semi-brittle fracture behavior of single-crystalline tungsten. They concluded that the behavior of micro-samples is more ductile with higher fracture toughness values compared to macro-sized single crystals. Similar conclusions were drawn by Ast et al. (2014) for NiAl. The fracture behavior of individual grain boundaries of an aluminum alloy was recently studied by combining crystal plasticity finite element simulation with cohesive zones and focused ion beam prepared microcantilevers (Kupka et al., 2014).

In this work, we combine experimental and numerical investigations in order to study the toughness of single-crystal small-scale tungsten samples. The development of the test procedure involves a new two-step fabrication procedure based on electrical discharge and focused ion beam machining. As an alternative to straight notches as used in Ast et al. (2014); Wurster et al. (2012), chevron notches were prepared, which offer, in particular at a small scale, the advantage of steady-state crack initiation and more controllable crack propagation under plane-strain conditions. In such small-scale fracture experiments the plastic deformation of the specimen during fracture cannot be neglected. To be able to distinguish between the contribution of plasticity and the contribution of cracking a finite element (FE) model was set up including crystal plasticity and cohesive zone elements. The comparison of the experimental results with the numerical ones allows for determining the toughness as well as orientation-specific effects of single-crystal tungsten for the crack system $\{011\}\langle 0\bar{1}1\rangle$.

2. Experimental approach

2.1. Method

Measuring the fracture toughness at the micrometer length scale requires a customized testing procedure, which differs from the standard fracture tests. Here, free-standing notched micro-cantilevers were tested using a nanoindenter (Nanoindenter G200 XP, Agilent, Inc.). To ensure comparability of the tungsten micro-cantilevers to macro-specimens, the sample geometry was based on the specifications of the standard ASTM sample and downscaled to maintain the proportions between the thickness W and the width B as well as the notch length a (Fig. 1). The notch was positioned close to the fixed end of the cantilever to minimize plasticity in the region between the fixed end and the notch. Two different notch geometries (Fig. 1) were investigated, i.e. the straight-through notch (STN) and the chevron notch (CN) (Schmitt et al., 2013), both experimentally and by simulation.

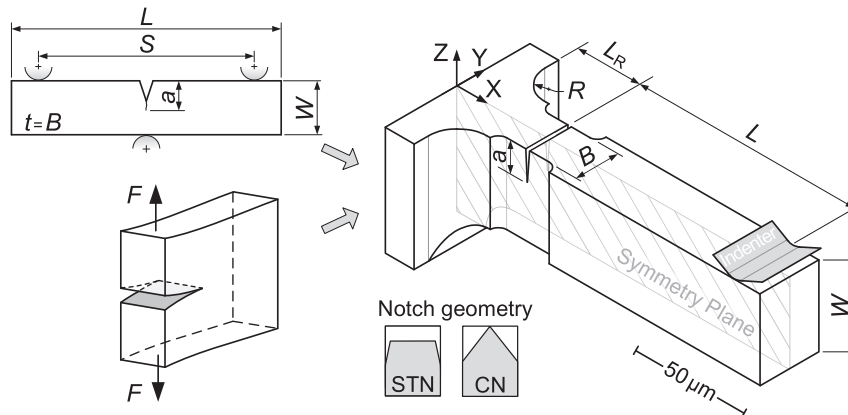


Fig. 1. Free-standing micro-bending geometry based on single edge notch bending mimicking crack opening mode I with straight (STN) and chevron notch (CN) geometries.

2.2. Sample preparation

The free-standing micro-cantilevers were manufactured following a two-step process using micro electrical discharge machining (μ -EDM) and focused ion beam (FIB) milling (Nova NanoLab 200, FEI Company). The bulk tungsten single crystal was carefully aligned in order to test the $\{011\}\langle\bar{0}11\rangle$ crack system (Fig. 2). First, the cantilevers were carved out of the bulk material by μ -EDM. A free-standing thin plate was created by two horizontal cuts parallel to the surface of the bulk material. Then, a row of cantilevers was prepared by several vertical cuts into the thin plate. The μ -EDM preparation leads to a rather rough surface and cracks near the surface both caused by re-deposition of the molten material and heat input. Therefore, FIB milling with decreasing beam currents from 20 nA to 0.5 nA was used to smoothen the cantilever sidewalls at the notches. Also, the notches were introduced by FIB machining. The final geometry of the cantilevers is shown Fig. 2 (a) and (b). The preparation procedure has been described in greater detail in Schmitt et al. (2013).

In Fig. 2(c) and (d) the STN and CN geometries, respectively, are shown. For the STN, the FIB cut was carried out perpendicular to the surface, which resulted in increased material removal at the edges of the cantilevers compared to the middle of the beam. For the CN, the gallium implantation due to the FIB machining is minimized, since the ion beam mills through the sample at an angle of 45° instead of milling into the material at 90° as is done in case of the STN. Also, the gallium implantation from the sidewall smoothing should be minimal since the ion beam worked like a chisel from the sides. These assumptions are supported by the work of Wurster et al. (2012), in which no difference in the fracture toughness of cantilever beams having both mechanically and FIB-prepared notches was observed.

The initial crack length can be determined very accurately in relation to the specimen width. In the experiments, however, the respective crack path (crack length) to the related force-displacement data could be detected only with difficulties and assumptions. This is also reflected by the large uncertainty of the K_Q values of tungsten micro-cantilevers (Schmitt et al., 2013), which were estimated via an energy relation and were in the range between 5.9 and 35 MPa m^{1/2} as the lower and upper limits. The force-displacement curves showed a rather ductile behavior and the crack propagated at a constant force until failure occurred (Schmitt et al., 2013). The characteristic shape of the force-displacement curve, though, with a load reduction at crack initiation typically observed in fracture experiments was not reported. It can be concluded that it is difficult

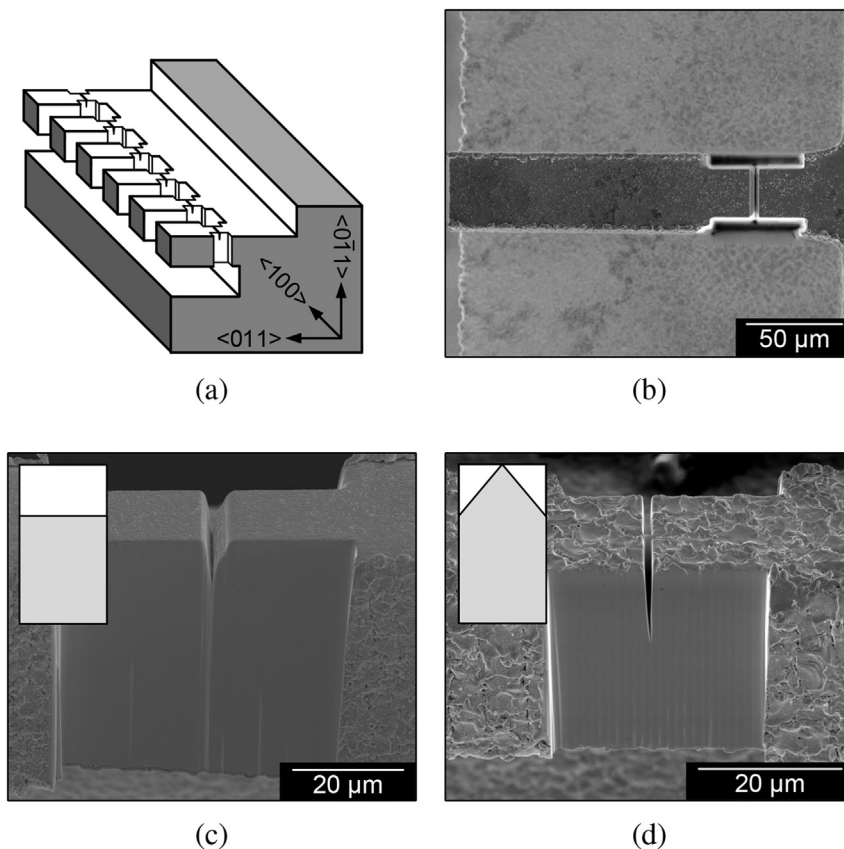


Fig. 2. Geometry of the cantilever beams. (a) The row of cantilevers was prepared by μ -EDM. (b) The notch was prepared by FIB milling close to the fixed end of the cantilevers. Two notch geometries were investigated, (c) straight notches and (d) chevron notches. The insets in (c) and (d) schematically show the cross sections at the notches. The cantilever sidewalls were smoothened by FIB milling in order to remove the damage layer from the μ -EDM.

to control the loading using micro-cantilevers with STN. Therefore, a chevron notch (CN) geometry was used in our further studies, which leads to steady-state crack propagation under plane-strain conditions and a more controllable loading situation. Also, a fatigue pre-crack is not needed (Brown, 1988). However, the initial crack length a_0 which is important for the experimental evaluation is no longer clearly defined by the chevron-shaped ligament. Nevertheless, chevron-notched specimens with a so called 'starter-notch' are increasingly used for fracture toughness testing of small scale specimens as well as for brittle-ductile materials such as tungsten (Brown and Baratta, 1992; Brown, 1988; Iqbal et al., 2012; Wurster et al., 2012).

2.3. Experimental observations

Using a nanoindenter, two types of experiments were conducted. The cantilevers were deflected to a predefined displacement, held at the maximum load for 10 s and unloaded or were loaded until fracture occurred. In addition, loading-unloading experiments with several cycles to increasing loads were carried out. Here, the cantilevers were deflected in predefined displacement increments and unloaded to 50% of the maximum force in the respective loading cycle. The beams were loaded at a displacement rate of 20 nm/s and unloaded at 1 mN/s. The STN cantilevers were deflected using a diamond Berkovich tip, while all other experiments were conducted with a 90°-wedge tip of 20 μm length. The Berkovich tip indented the beam surface during the bending experiment, which was avoided in case of the wedge tip. The relatively large contact area of the wedge tip prevents the tip penetration into the surface and also reduces the sliding of the tip at larger displacements. Also, mixed-mode loading is prevented, which is not unlikely to occur for the case of point-loading with a Berkovich tip (see Appendix A).

In Fig. 3(a) typical force-displacement curves of two STN cantilevers are shown. Both exhibit similar force-displacement behaviors. First, linear-elastic deformation is observed followed by an elastic–plastic transition and strain hardening. Then, in both cases a segment at constant force follows showing increasing displacement values before fracture occurred. In both cases, fracture started during the constant force segment, which indicates that unstable crack growth had occurred.

In Fig. 3(b) typical force-displacement curves of CN cantilevers are shown. The behavior of these beams at the beginning is similar to the cantilevers with straight notches. First, linear elastic deformation is observed followed by an elastic–plastic transition and strain hardening. Compared to the STN, in the segment at constant force the displacement increase is much more pronounced.

In case of the CN, the resistance to crack growth increases with increasing crack length due to the increasing area. Crack propagation at a constant load as observed in our experiments would thus lead to an increasing ΔK and stable crack growth until the crack has run completely through the notched area. During the constant load segment (indicated in Fig. 3(b)), a steep increase of the displacement rate can be seen (right axis, cross and plus symbols), which might indicate the transition to unstable crack growth. Fracture surfaces of STN and CN cantilevers are shown in Fig. 4(a) and (b), respectively. In Fig. 4(a), close to the notch, ripples can be seen (1). Further down, the fracture surface appears smooth (2), until noticeable roughness with river lines dominates (3) typical of brittle cleavage. The regions of the fracture surface in Fig. 4(b) are more clearly separated. There are three regions: the region influenced by the CN (1), a smooth (2) and a rough (3) region.

In Fig. 5(a) a force-displacement curve of a typical loading-unloading experiment is shown. An extended strain hardening region can be seen in Fig. 5(a). Then, the force continuously decreased with increasing number of loading cycles. The beam stiffness, as determined from the unloading portions of the curve, reflects this behavior (Fig. 5(a)). Three different regimes can be observed. In the first one, i.e. the elastic regime, no change in the stiffness can be seen. In the second regime, the stiffness decreases slightly, while in the third one, the stiffness decreases significantly accompanied by a notable decrease of the deflection force. The force and stiffness changes indicate the onset of stable crack growth as will be discussed in more detail below. The displacement rate is stable throughout the whole experiment confirming the stable character of crack

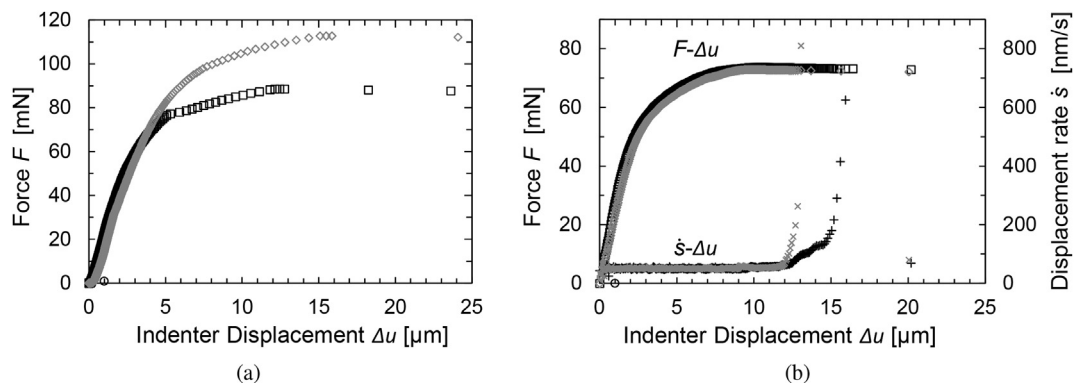


Fig. 3. Typical force-displacement curves of (a) STN cantilevers and (b) CN cantilevers.

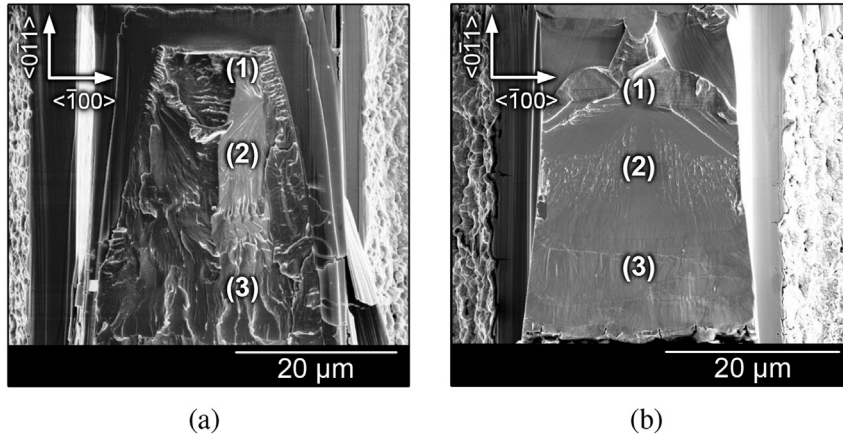


Fig. 4. Fracture surfaces of single-crystalline W cantilevers (a) with a STN and (b) a CN. Different features can be identified: ripples (1) as well as smooth (2) and rough (3) fracture surface.

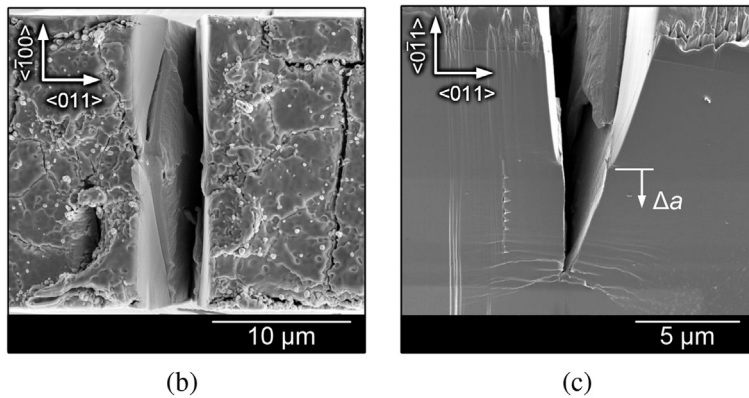
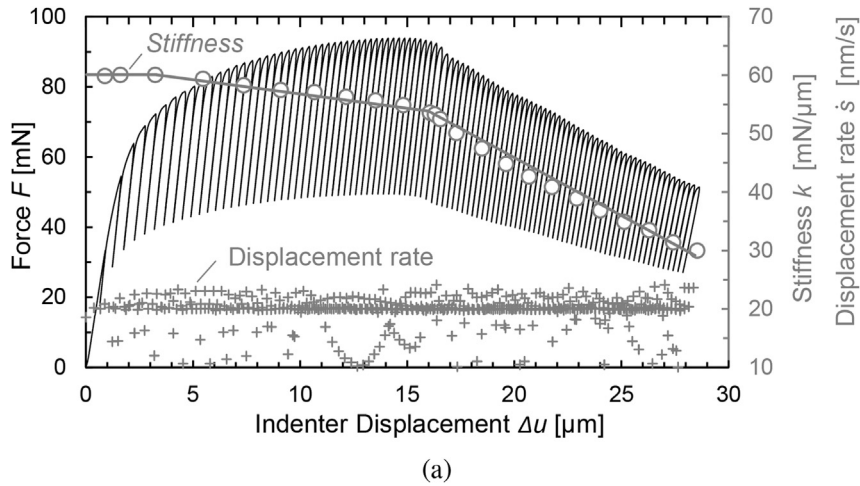


Fig. 5. (a) Force, stiffness (O) and displacement rate (+) vs. displacement of a CN cantilever (loading-unloading experiment). The beam fractured partially. (b) Top view and (c) side view of the notch region. The crack had already traversed the CN area, but the cantilever was unloaded before the crack had propagated completely through the beam.

propagation. Top and side-views of the notch region are shown in Fig. 5(b) and (c). As can be seen the crack had traversed the CN and had been propagating in a stable manner through the rest of the material.

The CN cantilever tested fractured only partially (Fig. 6) with significant plastic deformation of the cantilevers. In Fig. 6(a) the crack tip in a CN beam is shown; slip lines starting from the notch can be seen. These slip lines extend through the entire

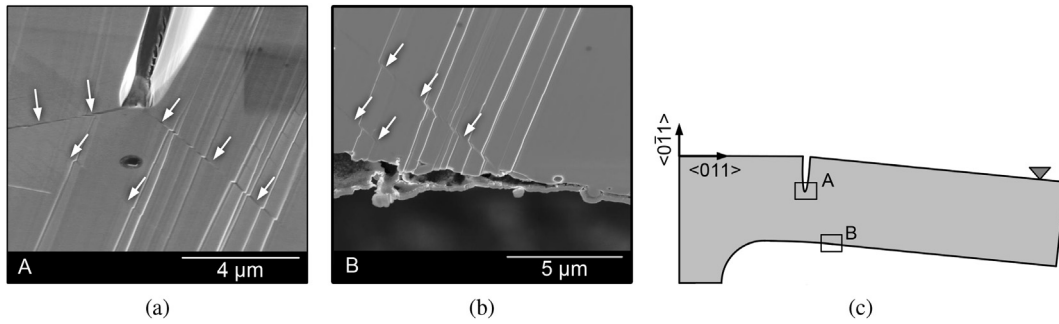


Fig. 6. Notch region of CN cantilever prior to fracture. The crack had almost reached the bottom of the CN. Slip lines, marked with arrows, can be seen at the ground of the notch in (a) and also at the lower edge of the cantilever in (b). The dislocation of the surface grooves confirms the occurrence of slip on specific slip planes and gives an indication on the amount slip. (c) Schematic showing the locations of the micrographs in (a) and (b).

thickness of the beam reaching the opposite surface (Fig. 6(b)). The extension of slip lines across the whole sample indicates that the size of the plastic zone has reached the sample size.

3. Numerical approach

3.1. Method

In this work a finite element crack growth model was developed in order to investigate the observed experimental behavior numerically. The plastic behaviour is described within the framework of crystal plasticity (Asaro, 1983) while cracking is mimicked by cohesive zone elements (Schwalbe et al., 2013) placed in the ligament. This approach allows to separate the contribution of the cracking process and of plasticity. One goal of the numerical study is to gain a better insight into the fracture process for the two different notch geometries CN and STN. Another one is to support the experimental study e.g. with adapted geometry functions or with crack growth predictions by using the compliance method. Furthermore, a comparison of experiment and simulation is performed which allows to determine the value of the fracture toughness.

Of course, tungsten single crystals deform plastically due to the movement of dislocations on distinct crystallographic planes. The resulting slip can be described in the framework of crystal plasticity. This constitutive law is based on Schmid's law (Schmid, 1931) where the resolved shear stress on the slip plane in slip direction is the driving force for crystallographic slip. If the resolved stress reaches a critical value, yielding starts, followed by hardening. In the present work we use the rate-dependent formulation of the crystal plasticity by Asaro (1983) to describe this behavior. However, it should be noted that Schmid's law describes the deformation of face-centered cubic single crystals very well while in body-centered cubic materials deviations from this law have been observed (Argon and Maloof, 1966; Marichal et al., 2014). This is due to the fact that in bcc metals the structure of the $\frac{1}{2}\langle 111 \rangle$ screw dislocation at the atomistic level is non-planar (Vitek, 2004). Most recently the resulting non-Schmid effect has been modelled via a modified Schmid tensor (Lee et al., 1999; Gröger et al., 2008a,b; Weinberger et al., 2012). As these more sophisticated models still cannot capture the yield behavior of a $[110]$ orientated tungsten single crystal, we chose to implement the pure Schmid formulation of Asaro (1983).

In this work, the purely local, phenomenological crystal plasticity model is used. Non-local plasticity theories that are able to represent dislocation fluxes (Sandfeld et al., 2013; Reuber et al., 2014) are required if (i) the slip length of a dislocation is larger than the finite element mesh or if dislocations even can leave the specimen (starvation) and (ii) complex multi-axial stress states dominate the system where statistically stored dislocations (SSDs) and geometrical necessary dislocations (GNDs) are converted into each other as e.g. during indentation (Reuber et al., 2014). These conditions are not applicable to our study, though, because of the cantilever beam dimensions and the rather simple deformation mode. Non-local strain gradient-based theories (Gao et al., 1999) can reproduce size-dependent hardening but the internal length scale parameter needs to be properly parametrized e.g. by experiments. These models are useful in situations that are dominated by plastic strain gradients (or arrays of GNDs, since $\rho^{GND} = (1/b)\nabla\gamma$ where γ is the plastic shear) in the low micro meter regime. We compute the internal length scale parameter l as used in well-established strain gradient plasticity models (Fleck and Hutchinson, 1993) based on the expression:

$$l = 3b\alpha^2 \left(\frac{\mu}{\sigma_y} \right)^2, \quad (1)$$

where $\sigma_y = 410$ MPa is the yield stress, $\alpha = 0.3$ is the Taylor hardening factor, $\mu = 160$ GPa is the shear modulus and $b = 0.27$ nm is the magnitude of the Burgers vector. With this it follows that $l \approx 11$ μm . Since this value is significant smaller than the size of our specimens, we conclude that size dependent behavior will only have a minor influence (which has also been acknowledged in the literature by e.g. Fleck and Hutchinson (1997) and Gao et al. (1999) for the size dependent system

response for different heights, which all indicate only a very small size dependent behaviour for systems of above $\approx 30 \mu\text{m}$). Coupling a cohesive zone model for fracture with a gradient crystal plasticity model (let alone a non-local, flux based model) has only rarely been attempted and still is far from being state of the art.

Cohesive zone models (CZM) represent one of the most widely used approaches to simulate numerical fracture processes from crack initiation to overall failure (Schwalbe et al., 2013). In this work, a partly constant traction separation law (TSL) developed by Scheider and Brocks (2003) was chosen where two cohesive parameters (the cohesive strength σ_0 and the critical separation δ_0) are sufficient to describe the cohesive element behavior. They are related to the separation energy Γ_0 via

$$\Gamma_0 = \sigma_0 \delta_0 \left(\frac{1}{2} - \frac{1}{3} \frac{\delta_1}{\delta_0} + \frac{1}{2} \frac{\delta_2}{\delta_0} \right) \quad (2)$$

with the shape parameters δ_1 and δ_2 . In order to avoid an unwanted elastic opening of the cohesive elements, it is recommended to have a high initial cohesive stiffness in the beginning. Here, the cohesive stiffness, K_{coh} is approximately given by

$$K_{coh} = \left(\frac{\partial \sigma}{\partial \delta} \right)_{\delta \rightarrow 0} = \frac{\sigma_0}{\delta_1} \quad (3)$$

and can be directly influenced by the shape parameter in the TSL (Scheider and Brocks, 2003). The initial compliance should be selected in such a way, that the cohesive stiffness is higher than the material stiffness. Since σ_0 is material-dependent, δ_1 should be chosen as small as required (Schwalbe et al., 2013).

3.2. Finite element model

The geometry of the specimen is shown in Fig. 1. Its width W is $40 \mu\text{m}$ with a thickness B of $22 \mu\text{m}$ and a crack length a_1 of $10 \mu\text{m}$. The proportions between width W , thickness B and crack length a are identical to the ones of the standard ASTM samples. The notched micro-cantilever is represented by the three dimensional finite element (FE) model shown in Fig. 7. Due to the symmetry of the crystal lattice and the geometry, only one half of the specimen is modeled and meshed with 8-node brick elements with linear function. This general element class is named C3D8 in the used FE code ABAQUS. Besides the symmetry conditions, all degrees of freedom of the nodes at the fixation area are blocked. The specimen is in contact with the wedge indenter which is modeled as a rigid body. The friction coefficient between specimen and wedge is assumed to be 0.2. In our numerical experiments, the wedge indenter is placed $110 \mu\text{m}$ away from the notch and moved with a speed of 20 nm/s (displacement-controlled) in the negative z -direction.

In Fig. 7(a) the crack ligament is marked as red zone ahead of the crack plane where the cohesive zone model (CZM) is implemented as user defined finite elements (UEL) developed at GKSS Research Centre Geesthacht by Scheider (2006). For the STN specimen, the crack plane is divided into two areas, a so-called *seam* for the notch and a CZM with implemented cohesive zone elements. In case of the CN specimens, the crack plane is divided in addition to the seam into slices, which are defined with a width of the elements. Thus, the cohesive zone elements can be implemented individually in an element-based way for each row in dependence of the notch geometry. Wavy crack fronts due to the manufacturing process (see Fig. 2(c)) can thus be considered.

A partly constant traction separation law (TSL) with the shape parameters $\delta_1 = 0.01 \delta_0$ and $\delta_2 = 0.75 \delta_0$ was chosen to mimic the fracture process at the crack tip. A reasonable value for Γ_0 can be taken from fracture tests performed by Riedle et al.

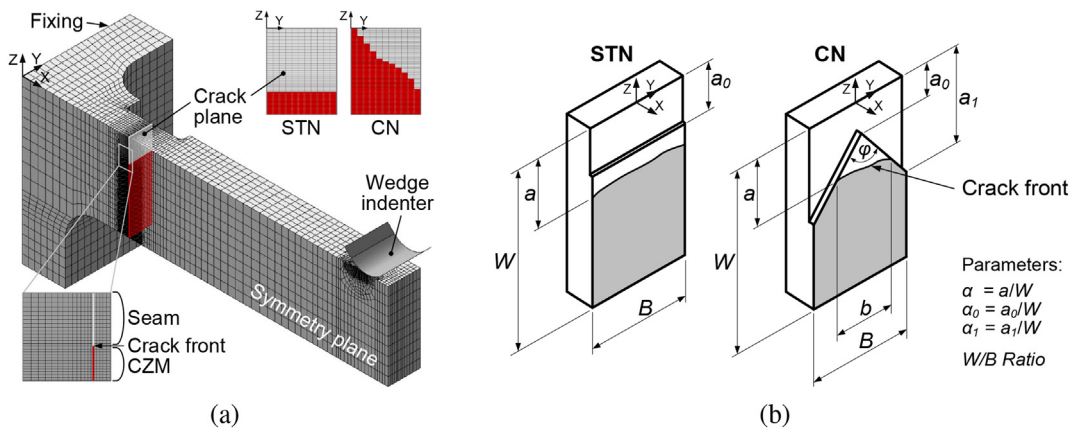


Fig. 7. (a) Three-dimensional finite element model of the micro-cantilever illustrating the mesh, the boundary conditions and the crack plane with cohesive zone elements. (b) Nomenclature and parameter definition for straight-through-notched (STN) and chevron-notched (CN) fracture specimens, accordingly to the used micro-cantilever geometry.

(1996) on tungsten single crystals on the macro-scale. They used the critical stress intensity factor K_{Ic} to characterize the anisotropic fracture properties, and obtained for each crack system an individual K_{Ic} . In our first parameter study, an average fracture toughness value of $K_{Ic} = 9.5 \text{ MPa m}^{1/2}$ was chosen. With the assumption, that the cohesive energy Γ_0 of the cohesive zone corresponds to the fracture toughness by Griffith's energy criterion (Griffith, 1921) and Irwin's stress intensity concept (Irwin, 1958)

$$\Gamma_0 = J_i \hat{=} G_{Ic} = \frac{K_{Ic}^2}{E'}, \quad (4)$$

a cohesive energy of $\Gamma_0 = 0.2 \text{ N/mm}$ is calculated under plane strain condition with $E' = E/(1 - \nu^2)$ and $E = 410 \text{ GPa}$ and $\nu = 0.28$. This value is kept to be the same. The cohesive strength σ_0 is taken to be 1500 MPa (about 3.6 times the macroscopic yield stress σ_Y). The corresponding critical separation δ_0 is then defined by the separation energy Equation (2). The length of one cohesive zone element l_c has to be smaller than δ_0 to avoid mesh sensitivity (Schwalbe et al., 2013). Another requirement stated by Schwalbe et al. (2013) is that the width of the adjacent continuum element b_c should be maximal $5 \times l_c$. Therefore, all simulations were performed with $l_c = 0.2 \text{ }\mu\text{m}$ und $b_c = 1 \text{ }\mu\text{m}$.

As plastic behavior can be observed at the crack tip (Fig. 6), crystal plasticity is implemented in the FE code ABAQUS using a user defined material (UMAT) written by Huang (1991). In this work any non-Schmid effects that may occur are neglected and the deformation is governed by slip only on $\{1\bar{1}0\}\langle 111 \rangle$ slip systems. Implementing just one slip system family in a bcc crystal such as tungsten is consistent with recent findings from atomistic and discrete dislocations simulations by Srivastava et al. (2013). They demonstrated that slip of a bcc crystal along high-index planes as often observed in experiments is obtained by the glide of the dislocation on two or more $\{110\}$ planes. The material parameters for the slip systems are taken from Yao (2012), namely the initial hardening modulus $h_0 = 1350 \text{ MPa}$, the initial yield stress $\tau_0 = 210 \text{ MPa}$ and the stage I stress $\tau_s = 530 \text{ MPa}$. These parameters are based on experimental nanoindentation tests on tungsten single crystals.

3.3. Numerical studies

3.3.1. Calculation of K_I and the geometry function

To determine the stress intensity factor (SIF) K_I from experimental force displacement curves a so-called *geometric function*, sometimes also called *shape function* is needed which depends on the crack geometry as well as on the loading situation. These relations have been compiled for many standard or practical geometries and loading conditions in handbooks, such as Sih (1973), Rooke (1976), Tada et al. (1985), Murakami (1986) and Fett and Munz (1994); Fett (2009). Murakami for example gives the following relations for a single edge cracked pure bending specimen (SEPB). With a bending moment of $M = F \cdot l$, the stress intensity factor K_I can be determined by

$$K_I = \frac{6M}{BW^2} \sqrt{\pi a} F(a/W) \quad (5)$$

with the geometry function $F(a/W)$ as

$$F(a/W) = C_0 + C_1(a/W) + C_2(a/W)^2 + C_3(a/W)^3 + C_4(a/W)^4. \quad (6)$$

Geometric functions for non-standard geometries are rarely available (Fett and Munz, 1994; Fett, 2009; Wu and Carlsson, 1991). Therefore, we determine them for our complex geometry numerically.

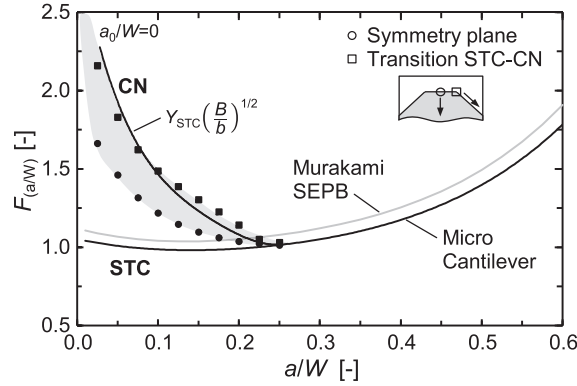
The finite model presented above ($B = 22 \text{ }\mu\text{m}$, $W = 40 \text{ }\mu\text{m}$) was simplified to perform this purely elastic analysis, namely by eliminating crystal plasticity and cohesive zones as the crack is described as non-propagating. In the STN and the CN specimens the crack length was varied between $0 \leq a/W \leq 0.6$, which was modelled via a seam as a sharp straight notch. The nomenclature used for a straight-through notch (STN) and a straight-sided chevron notch (CN) in a rectangular cross section is shown in Fig. 7(b). The crack length, a , and the specimen width, W , are measured from the front face of the micro-cantilever leading to the ratio $\alpha = a/W$. The dimension a_0 and a_1 are measured from the upper edge of the cantilever to the vertex of the CN and to the point where the CN intersects the specimen surface, respectively. The investigated CN specimens possess an initial crack ratio of $a_0/W = 0$ and $a_1/W = 0.25$.

From these elastic simulations, we obtain stress intensity factors K_I along the crack front for various a/W -ratios. As known in fracture mechanics, the K_I values are highest in the plane of symmetry due to plane strain conditions. Therefore, the average value K_I is taken to determine the geometry factors $F(a/W)$ (for known a/W -ratios) with Equation (5) which are then used to fit the parameters C_0 to C_4 of Equation (6) (given in Table 1). This procedure was applied to obtain $F(a/W)$ for micro cantilevers with straight notches (STN) and with chevron notches (CN).

The results are given in Fig. 8 together with Murakami's analytical geometric function values (grey solid line) using Equation (6) for different a/W -ratios. The black line represents Equation (6) fitted to the results obtained by FEM for STN. Due to its non-standard geometry, the curve is shifted parallel to Murakami's curve by a nearly constant value towards lower geometry factors, which consequently leads to smaller K_I values. The circle points in Fig. 8 correspond to the $F(a/W)$ value computed for the sample center in the CN and the rectangular points correspond to the values at the outer straight crack front as shown in the legend. Looking at the chevron notch in the range $0 \leq a/W \leq 0.25$, higher stress intensity factors can be

Table 1Geometry function parameters for the stress-intensity factor calculation with finite element fitting limits from $0 < a/W \leq 0.6$.

SEPB	C_0	C_1	C_2	C_3	C_4
Murakami (1986)	1.12	−1.40	7.33	−13.08	14.00
Fitted by FEM	1.05	−1.14	5.60	−9.33	10.92

**Fig. 8.** Comparison of stress intensity coefficients for chevron-notched (CN) and straight-through-notched (STN) crack specimens for different crack-length-to-width ratio a/W with $a_0/W = 0.0$ and $\phi = 90^\circ$.

observed, since the ligament width b in relation to specimen width B is very small. For a approaching a_1 , the chevron notch has a lower influence on the geometry factor and for $a \geq a_1$, $F(a/W)$ is equal for both samples (CN and STN).

The stress intensity factors of the two notch-shape geometries (STN and CN) are correlated to each other. In CN the straight crack front with an actual length a and width b are related to the sample width B and the crack length parameters a_0 and a_1 via the theorem on intersecting lines:

$$\frac{B}{b} = \frac{a_1 - a_0}{a - a_0}. \quad (7)$$

Using the assumptions of the general geometry function and that the change of compliance with crack length in a chevron-notched specimen was the same as the one for a straight-through crack specimen, Munz et al. (1980) obtained the correlation between K_{STN} and K_{CN} with

$$K_{CN} = K_{STN} \left(\frac{B}{b} \right)^{1/2} = K_{STN} \left(\frac{a_1 - a_0}{a - a_0} \right)^{1/2} \quad (8)$$

or

$$F(a/W) = F(a/W)_{STN} \left(\frac{B}{b} \right)^{1/2} = F(a/W)_{STN} \left(\frac{a_1 - a_0}{a - a_0} \right)^{1/2} \quad (9)$$

for $a_0 < a \leq a_1$.

Applying this relation on the numerically obtained $F(a/W)$ values of the STN specimens gives the solid curve at the upper gray area of Fig. 8. One can see that it corresponds approximately to the maximum values along the outer crack front obtained by FEM for CN specimens. For $a = a_0$, the geometric function (as well as the stress intensity factor) is very large and rapidly drops as the crack length increases to a minimum value. For $a \geq a_1$, the geometrical configurations are identical and the coefficients for the chevron-notched and straight-through-notched specimen are identical.

Overall, one can conclude that the analytical solution according to Murakami offers a good approximation. The corresponding parameters C_0 to C_4 for the geometry function $F(a/W)$ are listed in Table 1. However, the numerically obtained values for the investigated micro-cantilevers are slightly higher. The parameters for the micro-cantilevers, which were fitted by a polynomial function of fourth order to the numerical results, are also given in Table 1. To obtain the geometry function $F(a/W)$ in chevron-notched specimens in the range $a < a_1$ Equation (9) can be taken.

3.3.2. Compliance method

The compliance and accordingly the stiffness of notched specimens depend, among other factors, on the crack length. Therefore, periodic unloading-reloading sequences during the fracture test can be used to estimate the actual crack length (ASTM E1820-13, 2013; ASTM E561-10, 2013). A numerical study has been performed to understand how the experimentally

obtained stiffness k (defined by the slope of the unloading portions in the force-displacement diagram $k = \Delta F / \Delta u$, Fig. 5(a)) correlates with the crack length a .

The same elastic model as in the studies of the geometry function was used to study the stiffness behavior of STN and CN specimens with different initial crack length a . Again, the model refers to the standard geometry with $B \times W$ of $22 \times 40 \mu\text{m}^2$ and a/W varying from 0.05 to 0.6; a_0/W of 0 and a_1/W of 0.25 for CN specimens. In addition to the elastic study, the crack propagation model SX-CZM (presented in subsection 3.2) was applied to investigate the influence of non-straight crack fronts on the stiffness k in CN specimens. The stiffness k was thereby determined by several unloading-reloading sequences during cantilever bending as also done in experiments. Since the CN specimens show an approximately straight crack front for $a > a_1$, the simulation is not repeated for STN, as similar stiffness results can be expected for $a/W \geq 0.25$. However, another chevron-notched cantilever with $B = 25 \mu\text{m}$, $W = 44 \mu\text{m}$ and same a/W -ratios was modelled to investigate the geometry influence on the stiffness.

Fig. 9(a) shows the resulting stiffness k in dependence of the crack growth ratio a/W . The results of the elastic studies are shown as dashed lines for STN geometry in grey and for CN geometry in black, the solid lines represents the results from the crack propagation model (SX-CZM) for CN samples. The two CN geometries are marked with “ 22×40 ” and “ 25×44 ” with respect to the cross section. The cantilever with a larger cross section shows, as expected, a higher stiffness level at the beginning. In order to evaluate this influence, Fig. 9(b) shows the stiffness normalized by the initial stiffness k_{ini} of the notched cantilever (with $a/W = 0$) in percent over the crack propagation a/W .

A comparison between the results of the simpler elastic model with the more sophisticated crack propagation model (SX-CZM) reveals that the cantilever stiffness is not strongly affected by the separation of the cohesive zone in the FE-model and the deviations are negligibly small. The deviations mainly occur due the crack front variations of both models with different crack length definitions (elastic = straight crack front, SX-CZM = in the specimen center advancing crack front) as well as the relative movement between the indenter-tip and the surface. Similar to the experimentally found change in stiffness (see Fig. 5(a)), two different stiffness slopes sections can be identified in the numerical analysis of Fig. 9(a) with a transition at $a/W = 0.25$, where the chevron notch ends. Furthermore, it turns out that k scales with $B \cdot W^3$, as this product determines the area moment of inertia of a beam with a rectangular cross-section $B \times W$. Fig. 9(b) summarizes the results of the numerical study and it allows to relate experimentally observed stiffness reductions to the crack length a and consequently to crack growth Δa .

3.3.3. Notch geometry – study and crack resistance curves

The crack growth model (SX-CZM) was applied to simulate fracture in notched specimens with a crack orientation CO $\{011\}\{0\bar{1}1\}$. In this study, two different notch geometries were chosen, namely a straight-through notch (STN) and a chevron notch (CN). Both are modeled in Abaqus with a seam feature and a pre-crack of $a_0 = 10 \mu\text{m}$ ($a/W = 0.25$) for STN as well as $a_0 = 0$ and $a_1 = 10 \mu\text{m}$ for CN samples where B is $22 \mu\text{m}$ and W is $40 \mu\text{m}$. The indenter is moved with a speed of 20 nm/s in vertical direction. Fig. 10(a) shows the resulting force displacement curves obtained for the selected crystal orientation. If the cohesive stress σ_0 is reached in a CZM, the fracture process leads to a reduction in stiffness of the specimen which results in a decrease of the force F . The point of crack initiation is marked as $\Delta a = 0$ in Fig. 10(a) as well as the force values corresponding to the average crack growth of $\Delta a = 0.5; 1, 2, 4, 6, 8$ and $10 \mu\text{m}$. As their average crack length is smaller, chevron-notched micro-cantilevers have a higher force level than the straight-through notched cantilevers. In addition, the CN curve shows a stronger force reduction after crack initiation.

Besides the force-displacement curves the simulations give insight into the crack propagation. For both crack geometries, Fig. 10(b) shows the position and shape of the crack front ($\Delta a = 0.5$ to $10 \mu\text{m}$) due to increasing indenter displacement. Here, the following characteristics can be observed from the simulation. For the STN, as also observed experimentally, the crack

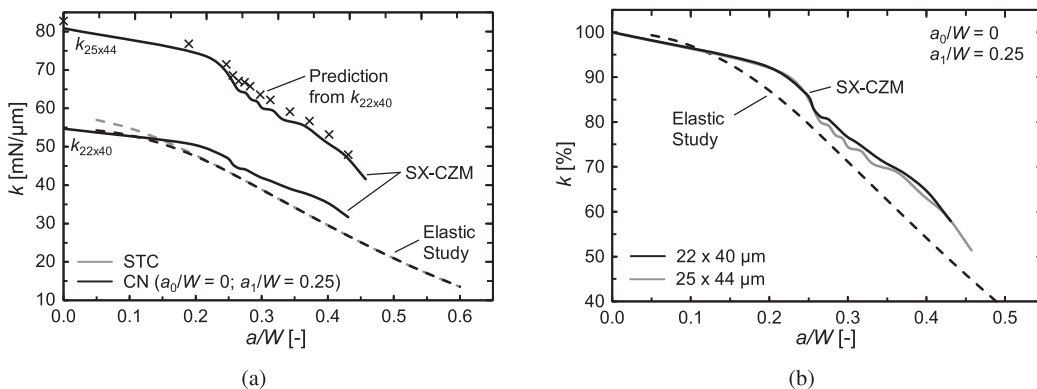


Fig. 9. (a) Stiffness behavior of STN and CN specimens in relation with the crack growth ratio a/W from elastic studies in comparison with two CN geometries simulated with crystal plasticity as constitutive law and cohesive zone elements. (b) Normalized stiffness behavior of the chevron-notched samples compared with two cross section geometries.

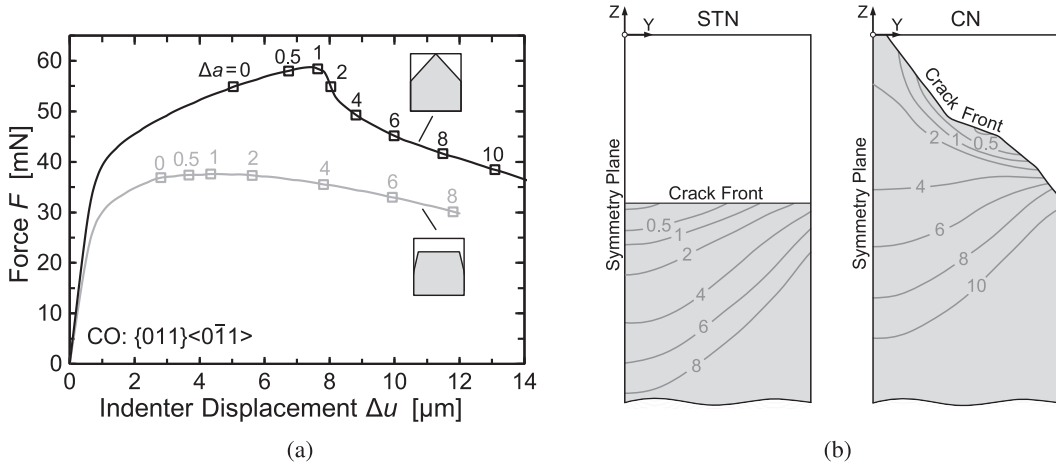


Fig. 10. (a) Force-displacement curves computed for the two notched cantilevers STN and CN with the cohesive parameters $\sigma_0 = 1500$ MPa, $\Gamma_0 = 0.2$ N/mm. Squares indicate the values for average crack growth Δa starting from crack initiation ($\Delta a = 0$) reaching Δa of 10 μm . (b) View on half of the crack ligament showing the current crack fronts for Δa ranging from 0.5 μm to 10 μm .

initiates in the center of the sample. This is due to the fact that in the bulk of the cantilever plane strain conditions dominate leading to higher stress triaxiality compared to the surface where plane stress conditions occur. The significant advancing crack in the sample center is characteristic for this crystal orientation. For CN, contrary to the expectation, the crack does not start in the symmetry plane. The initial crack front has not been modelled straight but owing to variation in the manufacturing process a bit wavy. At this weak point the crack initiation takes place. As soon as the crack reaches the sample center, a large number of elements fail instantaneously resulting in a strong reduction of the force ($\Delta a = 1$ to 2 μm). As Fig. 10(b) shows, this results in a straight crack (marked by 4 standing for $\Delta a = 4 \mu\text{m}$) which propagates similar to STN with increasing indenter displacement.

The fracture behavior can be characterized by crack resistance curves ($J - \Delta a$). In principle the J -Integral can be determined numerically. However, in accordance with Brocks and Scheider's findings (Brocks and Scheider, 2001, 2003), there is a strong numerical dependence of J_{num} with respect to the contour path, the meshing technique and the notch shape. Therefore, the J -Integral is determined from the computed force-displacement curve according to ASTM E1820-13 (2013) with basic test method calculations. Accordingly, J consists of an elastic J_{el} and plastic J_{pl} contribution with

$$J = J_{el} + J_{pl} = \frac{K^2(1 - \nu^2)}{E} + \frac{\eta A_{pl}}{B b_0} \quad (10)$$

where A_{pl} defines the plastic work of the applied load, B the net specimen thickness and b_0 is defined by the difference between the width W and the initial crack length a_0 . The non-dimensional η describes the effect of plastic work normalized by the ligament area and is defined with $\eta = 1.9$ for deep notches ($0.45 \leq a/W \leq 0.55$) (ASTM E1820-13, 2013). However, with initial a/W -ratios of 0.125 for chevron-notched and 0.25 for straight-notched specimens, relations from Nevalainen and Wallin (1994) for η are considered here. Based on a numerical fit to a number of different FEM solutions, Nevalainen and Wallin (1994) obtained a crack length dependent correlation of η with

$$\begin{aligned} \eta &= 13,818 \frac{a}{W} - 25,124 \left(\frac{a}{W} \right)^2 \quad \text{when } 0 < \frac{a}{W} \leq 0,274 \\ \eta &= 1,859 + \frac{0,03}{1 - \frac{a}{W}} \quad \text{when } 0,274 < \frac{a}{W} \leq 0,9 \end{aligned} \quad (11)$$

The crack growth Δa for STN and CN is determined for increments by adding up the total area of “broken” cohesive elements and dividing by the current net specimen thickness B_N , taking into account the transverse contraction of the volume. For CN specimens, an “effective” fracture surface A_{eff} for the chevron-notched fracture area is needed, since the fracture surface is defined too large according to ASTM with a height of $b_0 = W - a_0$ with $a_0 = 0$. The effective fracture surface was defined with

$$A_{eff} = B_N \cdot (a - a'_0) \quad (12)$$

where the initial crack length a'_0 is $a_1/2$, from where the crack growth Δa starts (see Fig. 11(b)). Thus, the crack growth Δa corresponds to the same resulting fracture surface and is comparable for both notch geometries. The stress intensity factor K

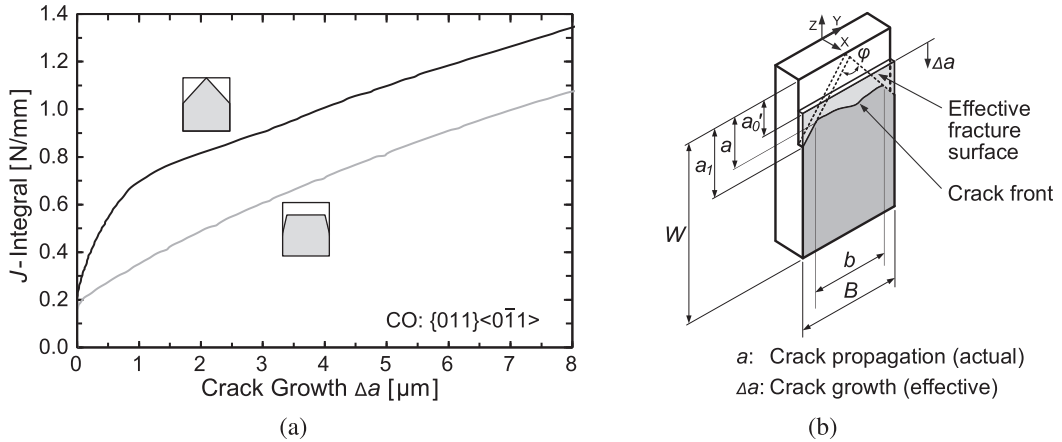


Fig. 11. (a) Crack resistance curves computed numerically for STN and CN cantilevers with $\{011\}\langle 011 \rangle$ crack system with $\Gamma_0 = 0.2 \text{ N/mm}$ and $\sigma_0 = 1500 \text{ MPa}$. (b) Modified effective fracture surface definition for chevron-notched fracture specimens.

for the elastic part of J is calculated using Equations (5) and (6) with taking account of the found parameters in Table 1 and according to Equation (10), where the chevron notch is considered. For straight-through-notched and chevron-notched specimens, the $J - \Delta a$ or $J - R$ curves are shown in Fig. 11(a). Due to the cohesive energy value $\Gamma_0 = 0.2 \text{ N/mm}$ used in both simulations crack initiation occurs at a J -value of 0.2 N/mm in all investigated cases.

After crack initiation the $J - R$ curves show different shapes, which is primarily caused by the respective notch geometry. The determination of the geometry function has already been shown that micro-cantilevers with chevron notches, compared to straight-through notched specimens, have a much higher value for the geometry function. These very disparate notch geometries lead at the beginning of growth to differences in plastic deformation within the process zone, which plays an important role for the J -Integral, since J is defined as the sum of J_{el} and J_{pl} . Here, the plastic component of J dominates and leads to higher values for chevron-notched specimens due to higher geometry function values. With an increasing fracture surface the influence from the chevron notch is becoming smaller and both curves show similar gradients. At crack propagation of about $\Delta a = 4 \mu\text{m}$ and larger, the deviation of the two curves is almost constant with a value of about $\Delta J = 0.25 \text{ N/mm}$.

4. Discussion

4.1. Comparison between experiment and simulation

The numerical study presented in Section 3 was performed on specimens with a sample width W of $40 \mu\text{m}$ and a thickness B of $22 \mu\text{m}$ while the experimental results shown in Fig. 4 originate from a sample with $W = 44 \mu\text{m}$, $B = 22 \mu\text{m}$ and an initial chevron notch crack length a_1 of $8.8 \mu\text{m}$. To be able to compare the computed and measured force-displacement curves quantitatively, the simulation of the micro bending test was repeated with adapted geometry ($W = 44 \mu\text{m}$, $B = 22 \mu\text{m}$, $a_1 = 8.8 \mu\text{m}$) by keeping the remaining parameters the same (e.g. $\Gamma_0 = 0.2 \text{ N/mm}$, $\sigma_0 = 1500 \text{ MPa}$). The higher width results in a stiffer behavior leading to a higher force level compared to Fig. 10(a). However, the experimental curve has still a higher maximum force than the numerical one. Therefore, further simulations were performed with varying values for the cohesive energy Γ_0 by keeping the cohesive strength σ_0 constant ($\sigma_0 = 1500 \text{ MPa}$). It turned out that a simulation with $\Gamma_0 = 0.37 \text{ N/mm}$ gives the same maximum force as found experimentally. Fig. 12(a) shows the resulting numerical force-displacement curve together with the experimental curve (of Fig. 4(a)). Additionally, the result of a simulation without cohesive zones is plotted as dashed line in Fig. 12 mimicking the purely elastic plastic behavior without crack propagation.

At first glance, the initial slopes of the solid curves deviate from each other. However, unloading-reloading sequences in the experiment reveal that the stiffness is actually in good agreement between simulation and experiment (marked by initial stiffness in Fig. 12(a)). The apparent deviation in stiffness during initial loading in the experiment is most likely caused by misalignment and/or micro-plastic deformation at the fixed end of the cantilever. Comparing to the experiment, yielding occurs earlier in the simulation followed by a somewhat stronger strain hardening. This implies that there is room for improvement with respect to the crystal plasticity model.

As the shape of the experimental and the numerical force displacement curves are similar, findings gained from the numerical analysis also hold for the experiment. One can conclude that the rapid reduction in the force found experimentally originates from the growth of the crack through the chevron notch until approximately a_1 is reached and a straight crack front is obtained (see Fig. 10). Then, the rapid reduction in force relates to further crack growth, which is stabilized by the unloading sequences and the displacement-controlled indenter motion. With increasing indenter displacement, plastic slip continues to occur leading to a ductile material behavior of tungsten even at room temperature. This is also confirmed by the rippled fracture surface which occurs by means of plastic deformation in addition to brittle cleavage (Schmitt et al., 2013).

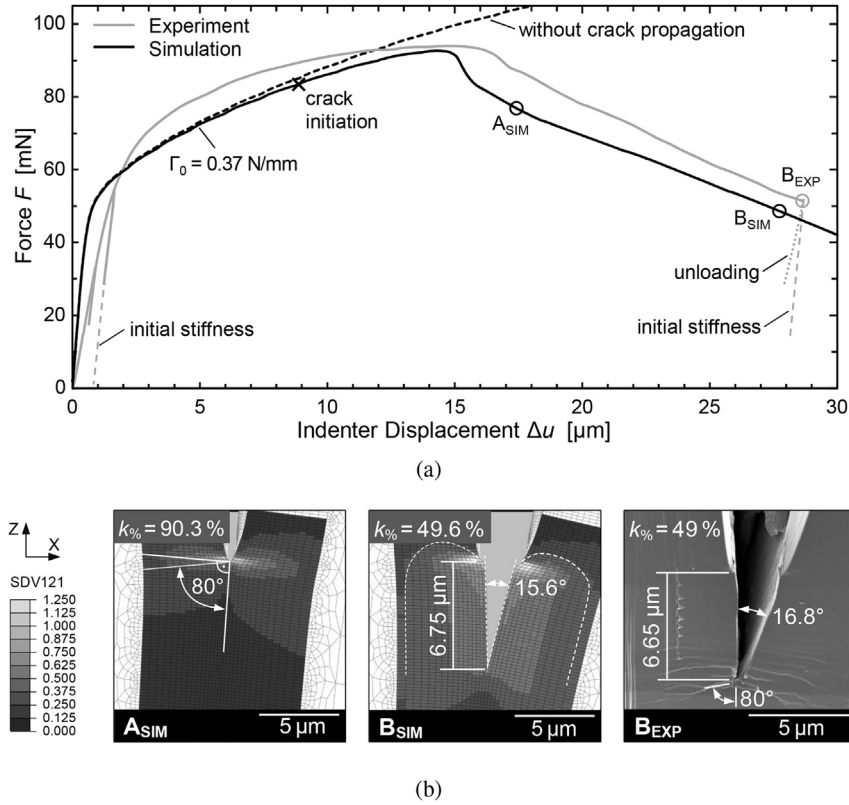


Fig. 12. Experimental and simulated behavior of a micro-cantilever specimen of single-crystal tungsten with $\{011\}\langle 0\bar{1}1\rangle$ -crack system; (a) Comparison of experimental and simulated force-displacement curves with characteristic marks for the crack growth analysis and an additional simulation curve without crack propagation; (b) Development of simulated crack growth on the surface and slip activities with an angle ϕ of about 80° and 90° at point A_{SIM} and B_{SIM} in comparison with the interrupted experiment at point B_{EXP} .

Besides the $F - \Delta u$ curve, the final crack length at the surface of the tested specimen can be used to evaluate the numerical approach. At point B_{EXP} in Fig. 12(a), a crack growth of $\Delta a_{surf} = 6.65 \mu m$ and a normalized stiffness $k\%$ of 49% is measured, see Fig. 12(b). At the same force (marked as B_{SIM} in Fig. 12) the numerical solution shows a $k\%$ of 49.6% and a crack growth of $6.75 \mu m$. The results show a very good agreement and confirm the applicability of the compliance method together with the normalized stiffness correlation given in Fig. 9(b). Furthermore, the numerical and experimental values of the crack tip opening angle (CTOA) with 15° and 16.8° agree reasonably well. The small deviation is most likely caused by the micro-cracks occurring in the experiment.

Furthermore, the computed slip activities can be compared with slip traces visible in SEM micrographs of the specimen near the end of loading (B_{EXP} of Fig. 12(b)). To get an idea of the size of the plastic zone the accumulated shear strain γ_{tot} was analyzed. As expected, the plastic zone is smaller in the symmetry plane than at the surface due to plane strain conditions (Bohnert et al., 2013, 2014). The plasticity is concentrated in the area around the crack. Fig. 12(b) shows the accumulated shear strain γ_{tot} (named SDV121 in the legend) at the surface at an indenter displacement of $17 \mu m$ (A_{SIM}) and at an indenter displacement of $27 \mu m$ (B_{SIM}). The main slip activities can be found at an angle ϕ of about 80° to 90° towards the crack path. This is also observed experimentally. In Fig. 5 and B_{EXP} of Fig. 12 slip traces are namely visible with an angle ϕ of about 80° .

It should be mentioned, that the cumulative shear strain is the sum of the contribution of all 12 individual slips systems of the slip family $\{110\}\langle 111\rangle$. Yet, most activities take place on the slip system $(0\bar{1}1)[111]$ and $(0\bar{1}1)[\bar{1}11]$ with an angle ϕ of 125° and 88° . Other slip systems have a smaller contribution to the cumulative shear strain. The process zone moves with the propagating crack leaving a plastified region in the form of an envelope curve along the crack edge. This wake is marked in Fig. 12(b) (B_{SIM}) as dashed white curve and corresponds to the experimentally one (B_{EXP}).

One can conclude that simulation and experiment agree very well. This means that 0.37 N/mm is most likely the critical J -Integral of a small tungsten single crystal with a $\{011\}\langle 0\bar{1}1\rangle$ crack orientation which corresponds to the fracture toughness value of $K_{Q\text{CZM}} = 12.9 \text{ MPa m}^{1/2}$ according to Equation (4). In macroscopic tests, Riedle et al. (1996) found the same value for this orientation. This finding implies that the experiments with miniaturized sample geometry deliver meaningful results when analyzed appropriately. Moreover, it can be concluded that no size effects occurs at the length scale investigated here. This seems to be reasonable since strong size effects in pillar-compression test are typically observed at dimensions below $10 \mu m$.

4.2. Experimental approach and analysis

As the combined (experiment and simulation) approach above is rather elaborate, it would be desirable to analyze the experimental data without FEM. According to the standard ASTM E399-12 (2012), a valid fracture toughness value is assumed with a straight crack front in the context of the linear elastic fracture mechanics (LEFM) within a 95% secant of the initial slope of the force-displacement curve. Applying Equation (5) and the geometry function parameters in Table 1 determined for SEPB-specimens, a value of $K_{Q\text{ LEFM}} = 7.6 \text{ MPa m}^{1/2}$ is obtained using this standard approach. However, using LEFM does not deliver a valid critical value but only a lower limit of the fracture toughness, as no large-scale yielding is taken into account. As the force-displacement curve shows a clearly proportion of plasticity, elastic–plastic fracture mechanics has to be applied.

To determine the experimental crack growth, the compliance method was used corresponding to the unloading-reloading sequences of the $F - \Delta u$ curve as shown in Fig. 5(a). With the consideration of the effective fracture surface of the chevron notch the crack propagation Δa can be determined by following relationship:

$$\begin{aligned} \Delta a &= \frac{a^2}{2a_1} \quad \text{when } \frac{a}{W} > \frac{a_1}{W} \\ \Delta a &= a - \frac{a_1}{2} \quad \text{when } \frac{a}{W} > \frac{a_1}{W}. \end{aligned} \quad (13)$$

To obtain the R -curve, the J -Integral was calculated from the sum of the elastic and plastic values according to Equation (10). Furthermore, Fig. 13(a) shows the experimental and numerical $J - \Delta a$ - curve with a linear trend line of the cracking resistance values. In the simulation Δa is calculated from the area of the broken cohesive zone elements. Therefore, no blunting is considered in the numerical curve while in the experimental tests blunting gives a contribution to Δa . This is the reason why the curves show a stronger deviation at the beginning.

In the standard test, blunting is considered with a so called construction line (blunting line) which is shifted in standardized approaches by 0.2 mm on the x -axis. However, this value cannot be applied for small samples. The parallel shift of the construction line by Δa is related to the crack tip opening displacement δ_t due to blunting via $\Delta a \sim \delta_t/2$ (Kuna, 2010). This crack opening displacement is shown with the two marked crack edges on the left side in Fig. 13(c), which are superimposed on the right side with the unloaded sample to identify the crack opening. With a crack opening angle of 90° , a crack opening displacement δ_t of $0.3 \text{ }\mu\text{m}$ was determined. Note that this value agrees well with the critical separation of the cohesive zone elements used in the ($\delta_0 = 0.286 \text{ }\mu\text{m}$). Consequently, the construction line is shifted parallel by $\Delta a \sim \delta_t/2 = 0.15 \text{ }\mu\text{m}$. The intersection with the trend line results in a crack resistance $J_{Q\text{ EXP}}$ of 0.4 N/mm , which corresponds to the critical crack resistance at initiation. With Equation (4) a fracture toughness of $K_{Q\text{ J EXP}} = 13.3 \text{ MPa m}^{1/2}$ is calculated.

For a valid evaluation of the fracture toughness calculation with $K_{J\text{ IC}} = (J_{\text{IC}} \cdot E')^{1/2}$, all relevant sample dimensions must be larger than a defined comparable plastic zone. Considering the plastic zone ahead of the crack tip, which is proportional to the initial size ligament ($W - a_0$) and the thickness B , the following relationship must be therefore taken into account:

$$B, W - a > 10 \frac{J_Q}{\sigma_Y}. \quad (14)$$

With a yield stress of 515 MPa ($\sigma_Y = \tau_s/P$ with $\tau_s = 210 \text{ MPa}$ and Schmid Factor $P = 0.408$) and $J = 0.4 \text{ N/mm}$, the characteristic parameter according to Equation (14) is calculated to $7.7 \text{ }\mu\text{m}$ and meets the definition of the ASTM standard test method with the minimum allowable sample size $B = 22 \text{ }\mu\text{m}$. Table 2 compiles all fracture toughness values obtained in this work for single crystalline tungsten with the $\{011\}\{0\bar{1}1\}$ -crack system. Due to the large plastic deformation $K_{Q\text{ LEFM}}$ is not a valid fracture toughness value. Furthermore, it should be noted that the presented combined as well as the experimental approaches to determine the fracture toughness are not restricted to the material tungsten. However, we have not yet applied it to other materials.

5. Conclusions

The fracture of single-crystalline tungsten with the $\{011\}\{0\bar{1}1\}$ -crack system was investigated experimentally and numerically by means of notched micro-cantilever bending tests. The specimens were prepared by a combined μ -EDM and FIB milling process. The micro-cantilevers were tested with a nanoindenter, which was used to bend the cantilever at a defined distance from the notch. Parallel to the experimental program, a finite element crack model was developed in which crystal plasticity was used as a constitutive law and cohesive zone elements are placed in the crack ligament to mimic the fracture process. The simulations of micro-bending enable a detailed analysis of the fracture process and support the experimental studies with modified geometry functions. Moreover, crack growth can be predicted by means of the compliance-method.

The FE-model was applied to study the influence of the notch shape on the fracture process. Two different notches were considered, i.e. a straight one and a chevron notch. It was shown that (i) the geometry function of the micro-cantilevers deviates for both notch shapes from the standard samples described in the literature, (ii) a greater crack driving force with

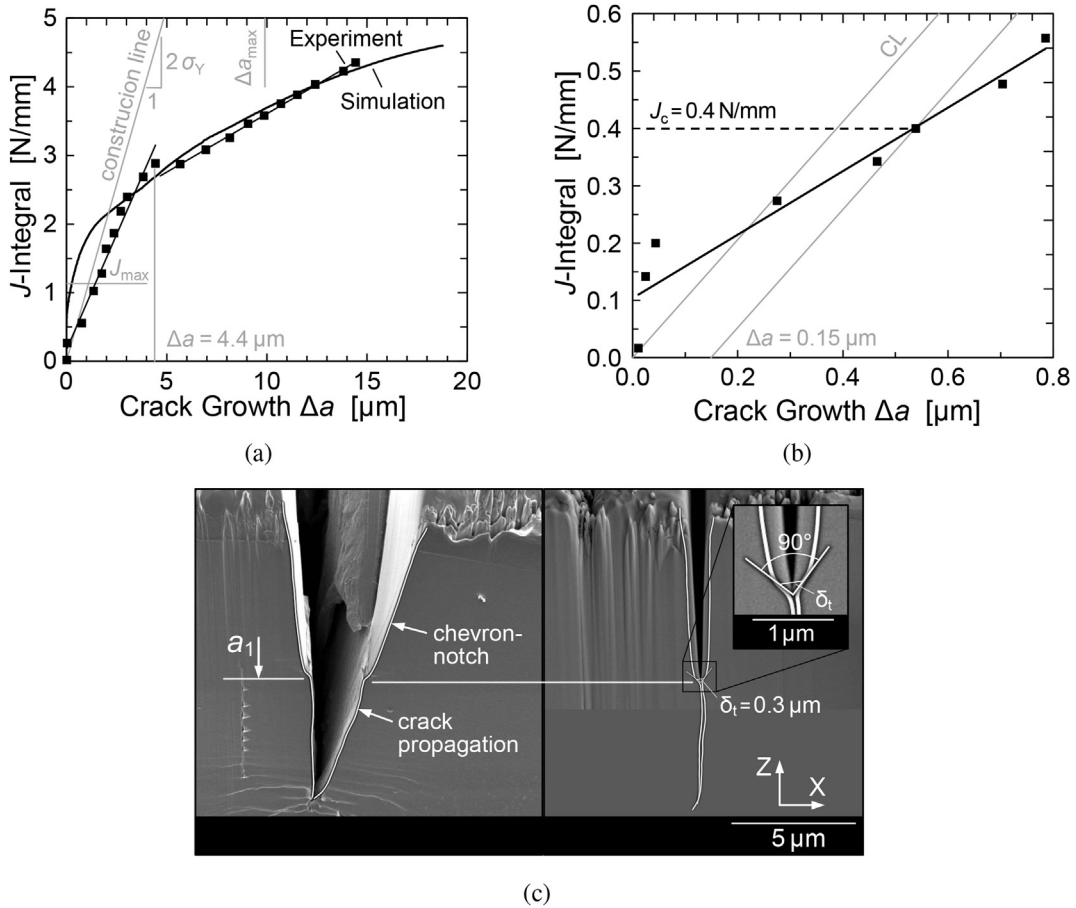


Fig. 13. (a) Comparison between simulation and experiment with the $J - \Delta a$ - curve to determine critical fracture-mechanic material parameters; (b) $J - \Delta a$ - curve at crack initiation with all evaluated data points corresponding to the unloading-reloading sequences of the experimental force-displacement curve; (c) Representation of the loaded and unloaded bending specimen to determine the blunting via the crack tip opening displacement δ_t .

Table 2

Experimentally and numerically determined fracture toughness on micro-cantilever specimens ($L = 110 \mu\text{m}$, $B = 22 \mu\text{m}$, $W = 44 \mu\text{m}$, $a_1 = 8.8 \mu\text{m}$) of single-crystal tungsten with $\{011\}\langle 0\bar{1}1 \rangle$ -crack system: $K_{Q \text{ LEFM}}$ determined (regardless of lack of standard conditions) by the LEFM; $K_{Q \text{ CZM}}$, determined in the combined approach simulation and experiment via the cohesive energy of the cohesive zone model and $K_{Q \text{ J EXP}}$ by $J_{Q \text{ EXP}}$ with appropriate crack tip blunting.

Crack system	$\frac{K_{Q \text{ LEFM}}}{[\text{MPa m}^{1/2}]}$	$\frac{K_{Q \text{ CZM}}}{[\text{MPa m}^{1/2}]}$	$\frac{K_{Q \text{ J EXP}}}{[\text{MPa m}^{1/2}]}$
$\{011\}\langle 0\bar{1}1 \rangle$	7.6	12.9	13.3

significantly higher shape function values results from the chevron notch, which are directly related to the shape function of the straight notch and (iii) the chevron notch has a reduced stiffness change with increasing crack length compared to the straight notch.

Furthermore, the newly developed crack model matches the experimental observations stemming from a chevron-notched specimen very well. Our approach combining experiment and simulation shows (i) approximately the same force-displacement curves, (ii) same slip activities in front of the crack tip and (iii) an identical crack growth at same rigidity. This approach allows to separate the contributions of the cracking process and of plasticity and to determine a value for the fracture toughness via the cohesive energy. This fracture energy value corresponds to the fracture energy value known from the literature at the macro-scale (Riedle et al., 1996). Finally, based on the combined approach, a purely experimental procedure was proposed where blunting is taken into account with a parallel shift of the construction line by $0.15 \mu\text{m}$. With this investigation, it was shown that the microscopic specimen dimensions do not significantly affect the fracture toughness. Thus, the fracture material parameters can be obtained from the testing of miniaturized samples despite a significant amount of plasticity, when the experiments are analyzed appropriately, and be transferred to the macroscopic scale.

Acknowledgments

The authors gratefully acknowledge the financial support by the State of Baden-Württemberg via the Postgraduate Research Grants Program: “Gefügestrukturanalyse und Prozessbewertung”. O.K. would like to thank the Robert-Bosch-Stiftung for partial financial support.

Appendix A. Indenter tip study – Cone vs. Wedge indenter (Bending of the micro-cantilever)

As the crack opens during bending, the cantilever moves relative to the indenter. To clarify this influence of the loading conditions on the stress field at the crack tip several linear elastic simulations were performed (Bohnert et al., 2013). It was found for different indenter tip geometries, that the samples are penetrated and scratched (differently) with the result of a lateral and a normal relative indenter movement. This relative movement caused (i) a deviation between the measured and the actual displacement and affects thus the force-displacement curves, (ii) the effective lever length between notch and load point is getting smaller and (iii) lateral forces results in the cantilever and influenced the crack opening mode. The simulations show that the force-displacement curves are affected in such a way that the error (e.g. for K or J -Integral calculation) can be up to 12% in case of an axisymmetric indenter tip geometry with a small radius. If only the displacement of the indenter tip is experimentally accessible, an indenter with a large contact area like a wedge indenter is recommended as localized penetration is prevented and the maximum error is minimized. In a further study of the crack opening mode it becomes clear that mode I is the dominant mode, the K_{II} value is about 6% of K_I .

References

- Argon, A.S., Maloof, S.R., 1966. Plastic deformation of tungsten single crystals at low temperatures. *Acta Metall.* 14 (11), 1449–1462.
- Asaro, R., 1983. Micromechanics of crystals and polycrystals. *Adv. Appl. Mech.* 23, 1–115.
- Ast, J., Przybilla, T., Maier, V., Durst, K., Göken, M., 2014. Microcantilever bending experiments in NiAl evaluation, size effects, and crack tip plasticity. *J. Mater. Res.* 29 (18), 2129–2140.
- ASTM E1820-13, 2013. Standard Test Method for Measurement of Fracture Toughness. ASTM International, West Conshohocken, PA, USA, pp. 1–54.
- ASTM E399-12, 2012. Standard Test Method for Linear-elastic Plane-strain Fracture Toughness K_{Ic} of Metallic Materials. ASTM International, West Conshohocken, PA, USA, pp. 1–33.
- ASTM E561-10, 2013. Standard Test Method for K-R Curve Determination. ASTM International, West Conshohocken, PA, USA, pp. 1–16.
- Bohnert, C., Weygand, S.M., Schmitt, N.J., Schwaiger, R., Kraft, O., 2013. Numerical investigation of the fracture behavior of tungsten at the micro scale. In: International Conf. on Fracture, ICF13, pp. 1–9.
- Bohnert, C., Weygand, S.M., Schmitt, N.J., Schwaiger, R., Kraft, O., 2014. Orientation dependence of the fracture behavior of single-crystal tungsten. *Procedia Mater. Sci.* 479–484.
- Brocks, W., Scheider, I., 2001. Numerical aspects of the path-dependence of the J-integral in incremental plasticity. *GKSS* 1, 1–33.
- Brocks, W., Scheider, I., 2003. Reliable J-values: numerical aspects of the path-dependence of the J-integral in incremental plasticity. *Materialprüfung* 45 (6), 264–275.
- Brown, K., 1988. The Chevron-notched Fracture Toughness Test. *ASTM Standardization News*, pp. 66–69.
- Brown, K., Baratta, F., 1992. STP 1172–Chevron-Notch Fracture Test Experience: Metals and Non-metals. ASTM International.
- Fett, T., 2009. Stress Intensity Factors, T-stresses, Weight Functions, sixth ed. KIT Scientific Publishing, Karlsruhe.
- Fett, T., Munz, D., 1994. Stress Intensity Factors and Weight Functions for One-dimensional Cracks. Report: KFK, 5290, Karlsruhe.
- Fleck, N., Hutchinson, J., 1993. A phenomenological theory for strain gradient effects in plasticity. *J. Mech. Phys. Solids* 41 (12), 1825–1857.
- Fleck, N., Hutchinson, J., 1997. Strain Gradient Plasticity. In: Vol. 33 of *Advances in Applied Mechanics*. Elsevier, pp. 295–361.
- Gao, H., Huang, Y., Nix, W., Hutchinson, J., 1999. Mechanism-based strain gradient plasticity i. theory. *J. Mech. Phys. Solids* 47 (6), 1239–1263.
- Gludovatz, B., Wurster, S., Hoffmann, A., Pippin, R., 2010. Fracture toughness of polycrystalline tungsten alloys. *Int. J. Refract. Metals Hard Mater.* 28 (6), 674–678.
- Griffith, A.A., 1921. The phenomena of rupture and flow in solids. *Philosophical transactions of the royal society a: mathematical. Phys. Eng. Sci.* 221, 163–198.
- Gröger, R., Bailey, A., Vitek, V., Nov. 2008. Multiscale modeling of plastic deformation of molybdenum and tungsten: I. Atomistic studies of the core structure and glide of 1/2111 screw dislocations at 0 K. *Acta Mater.* 56 (19), 5401–5411.
- Gröger, R., Racherla, V., Bassani, J., Vitek, V., Nov. 2008. Multiscale modeling of plastic deformation of molybdenum and tungsten: II. Yield criterion for single crystals based on atomistic studies of glide of 1/2111 screw dislocations. *Acta Mater.* 56 (19), 5412–5425.
- Gumbsch, P., 2003. Brittle fracture and the brittle-to-ductile transition of tungsten. *J. Nucl. Mater.* 323 (2–3), 304–312.
- Huang, Y., 1991. A User-material Subroutine Incorporating Single Crystal Plasticity in the ABAQUS Finite Element Program (Mech Report).
- Iqbal, F., Ast, J., Göken, M., Durst, K., 2012. In situ micro-cantilever tests to study fracture properties of NiAl single crystals. *Acta Mater.* 60 (3), 1193–1200.
- Irwin, G.R., 1958. Elasticity and Plasticity/Elastizität und Plastizität, vol. 3/6. Springer, Berlin, Heidelberg.
- Kaufmann, D., Mönig, R., Volkert, C., Kraft, O., 2011. Size dependent mechanical behaviour of tantalum. *Int. J. Plast.* 27 (3), 470–478.
- Kraft, O., Gruber, P.A., Mönig, R., Weygand, D., 2010. Plasticity in confined dimensions. *Annu. Rev. Mater. Res.* 40 (1), 293–317.
- Kraft, O., Schwaiger, R., Nix, W., 1998. Measurement of mechanical properties in small dimensions by microbeam deflection. In: *MRS Proceedings* 518.
- Kuna, M., 2010. Numerische Beanspruchungsanalyse von Rissen: Finite Elemente in der Bruchmechanik, second ed. Vieweg+Teubner Verlag, Wiesbaden.
- Kupka, D., Huber, N., Lilleodden, E., 2014. A combined experimental-numerical approach for elasto-plastic fracture of individual grain boundaries. *J. Mech. Phys. Solids* 64, 455–467.
- Kupka, D., Lilleodden, E.T., 2011. Mechanical testing of solid-solid interfaces at the microscale. *Exp. Mech.* 52 (6), 649–658.
- Lee, Y.J., Subhash, G., Ravichandran, G., 1999. Constitutive modeling of textured body-centered-cubic (bcc) polycrystals. *Int. J. Plast.* 15 (6), 625–645.
- Margevicius, R.W., Riedle, J., Gumbsch, P., 1999. Fracture toughness of polycrystalline tungsten under mode I and mixed mode I/II loading. *Mater. Sci. Eng. A* 270 (2), 197–209.
- Marichal, C., Srivastava, K., Weygand, D., Van Petegem, S., Grolimund, D., Gumbsch, P., Van Swygenhoven, H., 2014. Origin of anomalous slip in tungsten. *Phys. Rev. Lett.* 113 (2), 025501.
- Mueller, M., Pejchal, V., Žagar, G., Singh, A., Cantoni, M., Mortensen, A., 2015. Fracture toughness testing of nanocrystalline alumina and fused quartz using chevron-notched microbeams. *Acta Mater.* 86, 385–395.
- Munz, D., Bubsey, R.T., Srawley, J.E., Aug. 1980. Compliance and stress intensity coefficients for short bar specimens with chevron notches. *Int. J. Fract.* 16 (4), 359–374.
- Murakami, Y., 1986. *Stress Intensity Factors Handbook*. Pergamon Press, Oxford.

- Nevalainen, M., Wallin, K., 1994. The effect of crack depth and absolute thickness on fracture toughness of 3 PB specimens. In: European Conference on Fracture, ECF10, pp. 997–1006.
- Reiser, J., Rieth, M., Möslang, A., Dafferner, B., Hoffmann, A., Yi, X., Armstrong, D., 2013. Tungsten foil laminate for structural divertor applications tensile test properties of tungsten foil. *J. Nucl. Mater.* 434 (1–3), 357–366.
- Reuber, C., Eisenlohr, P., Roters, F., Raabe, D., 2014. Dislocation density distribution around an indent in single-crystalline nickel: comparing nonlocal crystal plasticity finite-element predictions with experiments. *Acta Mater.* 71, 333–348.
- Riedle, J., Gumbsch, P., Fischmeister, H., 1996. Cleavage anisotropy in tungsten single crystals. *Phys. Rev. Lett.* 76 (19), 3594–3597.
- Rooke, D., 1976. Compendium of Stress Intensity Factors. Her Majesty's Stationery Office, London.
- Rupp, D., Weygand, S., 2010. Anisotropic fracture behaviour and brittle-to-ductile transition of polycrystalline tungsten. *Philos. Mag.* 90 (30), 4055–4069.
- Sandfeld, S., Monavari, M., Zaiser, M., 2013. From systems of discrete dislocations to a continuous field description: stresses and averaging aspects. *Model. Simul. Mater. Sci. Eng.* 21 (8), 085006.
- Scheider, I., 2006. The cohesive model foundations and implementation. In: GKKS Research Centre Geesthacht, second ed. GKSS Research Centre Geesthacht.
- Scheider, I., Brocks, W., 2003. Simulation of cupcone fracture using the cohesive model. *Eng. Fract. Mech.* 70 (14), 1943–1961.
- Schmid, E., 1931. Beiträge zur Physik und Metallographie des Magnesiums. *Zeitschr. Elektrochem.* 37 (8–9), 447–459.
- Schmitt, N.J., Bohnert, C., Eberl, C., Kraft, O., Weygand, S.M., Schwaiger, R., 2013. Investigation of the fracture behavior of tungsten at the micro scale. In: ICF 13th International Conf. on Fracture, Beijing.
- Schwalbe, K.-H., Scheider, I., Cornec, A., 2013. Guidelines for Applying Cohesive Models to the Damage Behaviour of Engineering Materials and Structures. Springer, Berlin Heidelberg.
- Sih, G., 1973. Handbook of Stress Intensity Factors. Lehigh University, Bethlehem, PA.
- Srivastava, K., Groger, R., Weygand, D., Gumbsch, P., 2013. Dislocation motion in tungsten: atomistic input to discrete dislocation simulations. *Int. J. Plast.* 47, 126–142.
- Tada, H., Paris, P.C., Irwin, G.R., 1985. The Stress Analysis of Cracks Handbook, second ed. Paris Production Inc., St. Louis.
- Takashima, K., Ogura, A., Ichikawa, Y., Higo, Y., 2001. Anisotropic fracture behavior of electroless deposited Ni-P amorphous alloy thin films. In: MRS Proceedings 657.
- Vitek, V., 2004. Core structure of screw dislocations in body-centred cubic metals: relation to symmetry and interatomic bonding. *Philos. Mag.* 84 (3–5), 415–428.
- Weinberger, C.R., Battaile, C.C., Buchheit, T.E., Holm, E.A., Oct. 2012. Incorporating atomistic data of lattice friction into BCC crystal plasticity models. *Int. J. Plast.* 37, 16–30.
- Wu, X., Carlsson, A., 1991. Weight Functions and Stress Intensity Factor Solutions. Pergamon Press, Oxford.
- Wurster, S., Motz, C., Pippan, R., 2012. Characterization of the fracture toughness of micro-sized tungsten single crystal notched specimens. *Philos. Mag.* 92 (14), 1803–1825.
- Yao, W., 2012. Crystal Plasticity Study of Single Crystal Tungsten by Indentation Tests (Ph.D. thesis). Universität Ulm.